The Astrophysical Journal, 580:696–704, 2002 December 1

THE DETECTION OF PURE DARK MATTER OBJECTS WITH BENT MULTIPLY IMAGED RADIO JETS

R. Benton Metcalf
Institute of Astronomy, University of Cambridge, Cambridge CB3 0HA, UK
Received 2002 February 23; accepted 2002 July 29

ABSTRACT

When a gravitational lens produces two or more images of a quasar's radio jet the images can be compared to reveal the presence of small structures along one or more of the lines of sight. If mass is distributed smoothly on scales of $\lesssim 10^7\ M_\odot$, independent bends in the jet images on milliarcsecond scales will not be produced. All three of the well-collimated multiply imaged radio jets that have been mapped on milliarcsecond scales show some evidence of independent bends in their images. Using existing data, we model the lens system B1152+199 and show that it likely contains a substructure of mass $\sim 10^5$–$10^7\ h^{-1}\ M_\odot$ or a velocity dispersion of ~ 10 km s^{-1}. An alternative explanation is that an intrinsic bend in the jet is undetected in one image and magnified in the other. This explanation is disfavored, and future observations could remove any ambiguity that remains. The probability of a radio jet being bent by small-scale structure both inside and outside of the host lens is then investigated. The known populations of dwarf galaxies and globular clusters are far too small to make this probability acceptable. A previously unknown population of massive dark objects is needed. The standard cold dark matter model might be able to account for the observations if small mass halos are sufficiently compact. In other cosmological models where small-scale structure is suppressed, such as standard warm dark matter, the observed bent jets would be very unlikely to occur.

Subject headings: galaxies: jets — gravitational lensing — radio continuum: galaxies

1. INTRODUCTION

The standard Λ cold dark matter (CDM) cosmological model has been very successful in accounting for observations on scales larger than around a megaparsec. However, it appears that this model faces difficulties on the scales of galaxies and dwarf galaxies (van den Bosch et al. 2000). One such problem is that CDM simulations of the Local Group of galaxies predict an order of magnitude more dwarf galaxy halos with masses greater than $\sim 10^7\ M_\odot$ than there are observed satellites of the Milky Way (MW) and M31 (Moore et al. 1999; Klypin et al. 1999; Mateo 1998). These simulations predict that 10%–15% of the virial mass of a galaxy halo is in substructures of mass $\gtrsim 10^7\ M_\odot$.

This overprediction of dwarf halos could be a sign that there is something fundamentally wrong with the CDM model. Proposed explanations include warm dark matter (WDM), which smooths out small-scale structure in the early universe (see, e.g., Bode, Ostriker, & Turok 2001), unorthodox inflation models that break scale invariance (Kamionkowski & Liddle 2000), and self-interacting dark matter that causes substructures to evaporate within larger halos (Spergel & Steinhardt 2000). Alternatively, CDM could be correct and the small dark matter (DM) clumps could exist but not contain stars, so as to escape detection as observable dwarf galaxies. This situation can easily, perhaps inevitably, come about through the action of feedback processes (radiation and supernova winds) from the first generation of stars in the universe (see, e.g., Bullock, Kravtsov, & Weinberg 2000; Somerville 2002). For example, photoionization can prevent gas from cooling and thus inhibit star formation in halos that are too small to be self-shielding. Several authors (e.g., Metcalf 2002) have argued that the overabundance of DM clumps is likely to extend down to smaller masses and larger fractions of the halo mass than have thus far been accessible to numerical simulations. These nearly pure dark matter structures have largely been considered undetectable.

Gravitational microlensing by stars has been observed in the four-image system Q2237+0305 through the long-term variations of the optical flux ratios (Irwin et al. 1989; Witt, Mao, & Schechter 1995; Woźniak et al. 2000 and references therein). Mao & Schneider (1998) first proposed larger scale substructure as an explanation for the magnification ratios of the four-image quasar lenses B1422+231, which do not agree with any simple lens model. The modeling of B1422+231 has since been improved in Bradač et al. (2002) and Keeton (2002). It still appears that a substructure with a mass of 10^4–$10^7\ h^{-1}\ M_\odot$ near image A is required to explain the difference between the radio and optical flux ratios in this system. Metcalf & Madau (2001) showed that if CDM substructure exists, it could be detected through the magnification ratios of four-image quasar lenses. Concurrently, Chiba (2002) modeled three four-image lenses and showed that a significant amount of substructure was necessary to make their magnification ratios agree with simple smooth lens models. These ideas have been further investigated in Metcalf & Zhao (2002) and Dalal & Kochanek (2002). These studies all rely on the influence of substructure on magnification ratios. This is a promising approach, but it is strongly model dependent and susceptible to misinterpretation because of microlensing by ordinary stars in the lens galaxy.

It was also predicted in Metcalf & Madau (2001) that CDM substructure should occasionally distort multiply imaged radio jets on milliarcsecond scales. This distortion would not be reproduced in all the images, so it can be distinguished from structure in the jet itself. This effect had also been suggested by Wambsganss & Paczynski (1992) as a method for detecting a large abundance of $m \gtrsim 10^6\ M_\odot$ primordial black holes. Previous to this Blandford & Jaroszynski (1981) had considered the distortion of single

imaged radio jets as a probe of galaxies under the assumption that they are intrinsically straight. As will be demonstrated, the method considered here has the important advantages over magnification ratio methods of avoiding any confusion with microlensing and avoiding any strong dependence on the lens model.

In § 2 the observations of mapped multiply imaged radio jets are summarized. In § 3 general considerations related to modeling multiply imaged radio jets are discussed, and specific models for one particular case are presented. The interpretation of these results in terms of the level of small-scale structure in the universe is addressed in § 4. General discussion and conclusions are in § 5.

In this paper the Hubble parameter is $H_0 = 65\,h_{65}$ km s^{-1} Mpc^{-1}.[1] For quantities that do not have a simple dependence on H_0, a value $h_{65} = 1$ is used. The present average density of matter in the universe in units of the critical density is Ω_m, and the cosmological constant in the same units is Ω_Λ. The "concordance" cosmological model ($\Omega_m = 0.3$, $\Omega_\Lambda = 0.7$) will be assumed throughout.

2. OBSERVATIONS OF MULTIPLY IMAGED RADIO JETS

Several lensed QSO radio jets have been imaged on milliarcsecond scales with the Very Long Baseline Array (VLBA) and other Very Long Baseline Interferometer (VLBI) configurations (Garrett et al. 1994; King et al. 1997; Koopmans et al. 1999; Rusin et al. 2001; Xanthopoulos et al. 2000; Ros et al. 2000; Kemball, Patnaik, & Porcas 2001; Marlow et al. 2001; Rusin et al. 2002). In only three of these cases is the jet collimated enough and the resolution high enough that a bend or kink could in principle be detected.

The two-image gravitational lens B1152+199 was discovered in the CLASS radio survey, and follow-up observations were done on the Keck II Telescope (Myers et al. 1999). The images are separated by 1.″56, and the redshifts of the source and lens are $z_s = 1.019$ and $z_l = 0.439$, respectively. Subsequently, Rusin et al. (2002) observed B1152+199 using the *Hubble Space Telescope* (*HST*), the Multi-Element Radio-Linked Interferometer Network (MERLIN), and VLBA. In the *HST* observations a faint, indistinct lens galaxy can be seen along with a fainter object that is interpreted as a dwarf galaxy companion. With VLBI they were able to map the two images of the radio jet on milliarcsecond scales. They discovered that in image A the jet appears straight, while in image B it is bent. No formal constraint on the significance of this bend is given in Rusin et al. (2002), and further observations may be required to make the detection certain. For the purposes of this paper, we will take the observations at face value and assume that the bend is not an instrumental effect. In § 3.2 lensing explanations for this bend are investigated. The bend is clearly not aligned with the direction to either image A or the lens galaxy. Superluminal motion is a possible explanation only if the jet's shape can change on a timescale that is smaller than the time delay between images. Rusin et al. (2002) fit a variety of smooth models to the macroscopic lens and get time delays of 41.1–70.6 h_{65}^{-1} days, which makes this an unlikely explanation. They do not attempt to explain the bend with their lens models.

The four-image lens MG J0414+0534 was observed with global VLBI by Ros et al. (2000). The jet consists of a two-component core and two radio lobes on either side. In images A2 and B all the radio components are nearly collinear, while in image A1 they are drastically misaligned. Only two components are detected in image C so in this case the alignment cannot be determined. The distortion of image A1 could be caused by a substructure near the image, or it might be due to the magnification of a small misalignment in the other images (see § 3.2.1). The situation will be clarified with further modeling of this particular source.

The double quasar Q0957+561 was the first gravitational lens discovered (Walsh, Carswell, & Weymann 1979) and has been studied extensively in the past two decades. The VLBI maps of the radio jets appear to show a kink in image A that is not reproduced in image B (near $\Delta\delta = 20$ mas, $\Delta\alpha = 10$ mas with respect to the core; Garrett et al. 1994; Barkana et al. 1999). Although in this case the bend is much less certain than in B1152+199 or MG J0414+0534—and we will not try to reproduce it with a lens model here—it does suggest that milliarcsecond kinks and bends are common. This has very important consequences in relation to the discussion in § 4 because it implies that the bend in B1152+199 is not just a rare coincidental alignment of the image and a known type of substructure.

3. MODELING THE JET

3.1. *Formalism*

The radio jet will be treated as a one-dimensional curve on the sky described by $\boldsymbol{\theta}_{\rm source}(s)$ in the absence of lensing. An image of the jet is described by $\boldsymbol{\theta}_{\rm source}(s)$. The curve of the source jet is related to the curve of its image through the lensing equation

$$\boldsymbol{y}(s) = \boldsymbol{x}(s) - \boldsymbol{\nabla}\psi[\boldsymbol{x}(s)]\ , \tag{1}$$

$$\boldsymbol{y}(s) \equiv \frac{D_l \boldsymbol{\theta}_{\rm source}(s)}{\lambda_0}, \quad \boldsymbol{x}(s) \equiv \frac{D_l \boldsymbol{\theta}_{\rm source}(s)}{\lambda_0}\ , \tag{2}$$

where λ_0 is an arbitrary scaling length and s is the arc length along the jet in the image plane measured in the same units as $\boldsymbol{x}$. The angular size distances to the lens, source, and from the lens to the source will be denoted D_l, D_s, and D_{ls}, respectively. The lensing potential is related to the lens surface density $\Sigma(\boldsymbol{x})$ through the Poisson equation $\nabla^2\psi(\boldsymbol{x}) = 2\kappa(\boldsymbol{x})$, where $\kappa \equiv \Sigma(\boldsymbol{x})/\Sigma_c$. The critical surface density is defined as $\Sigma_c = (4\pi G D_l D_{ls}/c^2 D_s)^{-1}$.

The tangent and normal vectors of the jet are given by

$$\boldsymbol{t}(s) \equiv \frac{\partial \boldsymbol{x}}{\partial s}, \quad \boldsymbol{n}(s) \equiv \frac{\partial^2 \boldsymbol{x}}{\partial s^2}\ . \tag{3}$$

The magnitudes of these vectors are $t(s) = 1$ and $n(s) = 1/R(s)$, where $R(s)$ is the radius of curvature. For convenience, we define the matrices

$$\mathbf{A}_{ij} \equiv \delta_{ij} - \frac{\partial^2\psi}{\partial x^i \partial x^j}, \quad \mathbf{M}_{ijk} \equiv -\frac{\partial^3\psi}{\partial x^i \partial x^j \partial x^k}\ . \tag{4}$$

Now we can find the curvature and normal vectors to the

[1] On a couple of occasions when quoting other peoples work the convention $H_0 = 100\,h$ km s^{-1} Mpc^{-1} is used.

source jet by taking derivatives of the lens equation

$$\boldsymbol{T}(s) \equiv \frac{\partial \boldsymbol{y}}{\partial s'} = \frac{\partial s}{\partial s'}\frac{\partial \boldsymbol{y}}{\partial s} = \frac{\boldsymbol{u}}{|\boldsymbol{u}|} , \tag{5}$$

$$\boldsymbol{N}(s) \equiv \frac{\partial^2 \boldsymbol{y}}{\partial s'^2} = \left(\frac{\partial s}{\partial s'}\right)^2 \frac{\partial^2 \boldsymbol{y}}{\partial s^2} + \frac{\partial^2 s}{\partial s'^2}\frac{\partial \boldsymbol{y}}{\partial s} = \frac{1}{|\boldsymbol{u}|^2}\left[\boldsymbol{v} - \frac{\boldsymbol{u}(\boldsymbol{v}\cdot\boldsymbol{u})}{|\boldsymbol{u}|^2}\right] , \tag{6}$$

$$\boldsymbol{u}_i \equiv \sum_j \mathbf{A}_{ij}\boldsymbol{t}_j, \quad \boldsymbol{v}_i \equiv \sum_j \mathbf{A}_{ij}\boldsymbol{n}_j + \sum_{jk} \mathbf{M}_{ijk}\boldsymbol{t}_j\boldsymbol{t}_k , \tag{7}$$

where s' is the arc length on the source plane. The vectors $\boldsymbol{T}(s)$ and $\boldsymbol{N}(s)$ must be the same for all images of the jet so they can be used as constraints on the lens model. Along with the position coordinates on the source plane this makes four constraints per point on the jet [$\boldsymbol{T}(s)$ and $\boldsymbol{N}(s)$ must be perpendicular and $|\boldsymbol{T}(s)| = 1$].

Let us estimate the relative size of the terms in equatiion (6). For any spherically symmetric lens, the Einstein ring radius $\lambda_{\rm E}$ is the solution to

$$\lambda_{\rm E}^2 = \frac{M(\lambda_{\rm E})}{\pi\Sigma_c} , \tag{8}$$

where $M(\lambda_{\rm E})$ is the mass within a projected distance of $\lambda_{\rm E}$. Images that are significantly magnified form near the Einstein radius for a spherical lens or, more generally, near critical curves (the curve $\boldsymbol{x}$ where $\det[\boldsymbol{A}(\boldsymbol{x})] = 0$). The magnitude of the deflection angle near $\lambda_{\rm E}$ is $\alpha(x) \sim \lambda_{\rm E}/\lambda_0$ so if an image is formed both near the Einstein radius of a host halo and near the Einstein radius of a subclump, their contributions to the deflection will differ by a factor of $\sim\lambda_{\rm E}^{\rm clump}/\lambda_{\rm E}^{\rm host} \sim (\sigma_{\rm clump}/\sigma_{\rm host})^2$. The matrices (eq. [4]) involve further derivatives of the lensing potential so that at the same point the two contributions to $\mathbf{A}_{ij}(\boldsymbol{x})$ will be roughly equivalent, while the contribution to $\mathbf{M}_{ijk}$ from the subclump will be larger than the host's by a factor of $\sim\lambda_{\rm E}^{\rm host}/\lambda_{\rm E}^{\rm clump} \sim (\sigma_{\rm host}/\sigma_{\rm clump})^2 \sim M_{\rm host}/m_{\rm sub}$. For dwarf galaxy–sized substructures, this is ~100–10,000. From equation (6) we see that to generate a curvature radius of order of the jet size λ_s, $\lambda_s\mathbf{M}_{ijk}/(\lambda_0|u|)$ needs to be $\gtrsim 1$. Roughly speaking, only objects with Einstein radii of order of the source size can create a noticeable bend.

As a working definition we will say that substructure is present in the lens when the bending matrix $\mathbf{M}$ in equation (6) is important. The effect of a smooth lens on the shape of a small source can then be describe by the magnification matrix $\mathbf{A}$ alone. This definition will clearly be dependent on the size of the source and the resolution of the observations.

If we believe that a significant gravitational bending of a jet is rare enough that it is unlikely to happen to both of a pair of images (at least at the same point on the jet), then the equations can be significantly simplified. The image without substructure will be labeled image 2. By expanding the lensing equation (1) around a point on image 1 and the corresponding point on image 2 and equating the position on the source plane, we can arrive at an equation analogous to equation (6) but relating the curvature of one jet image to the curvature of the other:

$$\boldsymbol{n}^{(2)} = \frac{1}{|\tilde{\boldsymbol{u}}|^2}\left[\tilde{v} - \frac{\tilde{\boldsymbol{u}}(\tilde{\boldsymbol{v}}\cdot\tilde{\boldsymbol{u}})}{|\tilde{\boldsymbol{u}}|^2}\right] . \tag{9}$$

The tildes signify the quantities in equation (7) only with the matrices $\tilde{\mathbf{A}} = \mathbf{A}_{(2)}^{-1}\mathbf{A}_{(1)}$ and $\tilde{\mathbf{M}} = \mathbf{A}_{(2)}^{-1}\mathbf{M}_{(1)}$ substituted.

We can see from equation (9) that in the absence of substructure a jet that is straight in one of its images will also be straight in its other images. However, the intrinsic curvature of the jet can be magnified or demagnified without substructure. In some cases the curvature could be observed in one image but be too small in another image to be detected, resulting in the erroneous conclusion that substructure must be present. For this reason, it is important to quantify by how much the curvature can be changed without substructure. In this case $\tilde{\boldsymbol{M}} = 0$, and from equation (9) we can find the *curvature magnification factor*:

$$C \equiv \frac{|\boldsymbol{n}^{(2)}|}{|\boldsymbol{n}^{(1)}|} = \frac{1}{|\tilde{\boldsymbol{u}}|^2}\left[|\tilde{\boldsymbol{v}}^*|^2 - \frac{(\tilde{\boldsymbol{v}}^*\cdot\tilde{\boldsymbol{u}})^2}{|\tilde{\boldsymbol{u}}|^2}\right]^{1/2} , \tag{10}$$

where $\tilde{\boldsymbol{v}}^*$ is $\tilde{\boldsymbol{v}}$ with $\boldsymbol{n}^{(1)}$ replaced with the unit vector $\tilde{\boldsymbol{n}}^{(1)}$. This quantity can be calculated with a smooth lens model fitted to the image positions and the tangent vectors to the jet images.

It is useful to have concrete models for the lenses. For a spherically symmetric lens with a power-law mass profile [$M(r) \propto r^n$], or at least a power law near the location of the image, the matrices (eq. [4]) can be calculated directly:

$$\alpha(\tilde{\boldsymbol{x}}) = \frac{\lambda_{\rm E}}{\lambda_0}\frac{\tilde{\boldsymbol{x}}}{\tilde{x}^{2-n}} , \tag{11}$$

$$\mathbf{A}_{ij} = \delta_{ij} - \frac{1}{\tilde{x}^{2-n}}\left[\delta_{ij} - (2-n)\frac{\tilde{x}^i\tilde{x}^j}{\tilde{x}^2}\right] , \tag{12}$$

$$\mathbf{M}_{ijk} = \left(\frac{\lambda_0}{\lambda_{\rm E}}\right)\frac{(2-n)}{\tilde{x}^{3-n}}\left[\frac{\delta_{ij}\tilde{x}^k + \delta_{ik}\tilde{x}^j + \delta_{jk}\tilde{x}^i}{\tilde{x}} - (4-n)\frac{\tilde{x}^i\tilde{x}^j\tilde{x}^k}{\tilde{x}^3}\right] , \tag{13}$$

where $\tilde{\boldsymbol{x}} \equiv (\boldsymbol{x} - \boldsymbol{x}_0)\lambda_0/\lambda_{\rm E}$ is the image position relative to the center of the lens. Also useful is the convergence or dimensionless surface density at the Einstein radius in these power-law models: $\kappa(\lambda_{\rm E}) = n/2$. For a singular isothermal sphere (SIS) lens, $n = 1$ and

$$\lambda_{\rm E} = 4\pi\left(\frac{\sigma}{c}\right)^2\frac{D_l D_{ls}}{D_s}, \quad \rho(r) = \frac{\sigma^2}{2\pi G r^2} . \tag{14}$$

For a point mass, $n = 0$ and $\lambda_{\rm E} = [m/(\pi\Sigma_c)]^{1/2}$.

As an example, Figure 1 shows the curvature magnification factor C for an SIS lens with no substructure. This quantity depends on both the position of the source and the tangent vector to one of the images (in this case the outer image is chosen). The factor is generally larger for jets that are radial (in which case the outer image is more bent) or tangential (where the opposite is true). Cases with C much different from 1 tend to have smaller magnification factors in the sense that the outer image is much brighter. Because of this, there will be a bias toward cases in which C is near 1. To fit real lens system, a more complicated, asymmetric lens model must be used and C must be calculated for each pair of images separately. This quantity can be evaluated at the center of a jet image or at a kink in a jet image to determine if the bend is consistent with an intrinsic feature in the jet itself or requires substructure as an explanation.

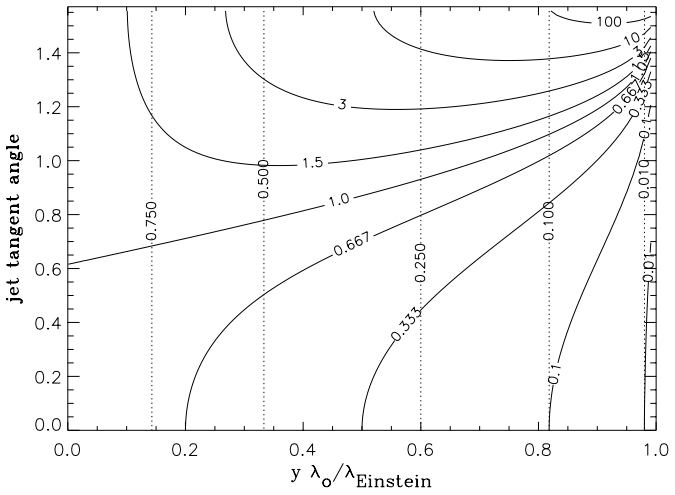

FIG. 1.—Curvature magnification factor (10; *solid contours*) for a singular isothermal sphere as a function of the radial position of the source in Einstein ring radii and the tangent vector to the outer jet image. The source position y is the magnitude of the vector defined in eq. (1). The tangent angle is defined so that zero is a radial jet and $\pi/2$ is tangentially oriented. For $C > 1$, the inner image is more curved, and for $C < 1$, the opposite is true. For $y\lambda_0 > \lambda_E$, there is only one image. The dotted contours show absolute value of the magnification ratio of the inner image to the outer image.

3.2. *Modeling of B1152+199*

Two explanations for the apparent bend in image B of B1152+199 will be explored. One is that image A actually has a small undetected curvature that is magnified in image B where it is detected. The second explanation is that image A is straight and image B is bent by the influence of a substructure near it. Investigating both of these hypotheses requires fitting a host lens model to the positions of the images and the center of the lens. Since there are only two images in this case, a complicated host lens model is not well constrained by the positions alone. Rusin et al. (2002) fitted to each VLBI image a point source for the core and a Gaussian for the jet; these positions are used as constraints. We choose to use a simple SIS model with a background shear—$\alpha^1(\boldsymbol{x}) = \gamma[x^1\cos(2\theta_\gamma) + x^2\sin(2\theta_\gamma)]$, $\alpha^2(\boldsymbol{x}) = \gamma[x^1\sin(2\theta_\gamma) - x^2\cos(2\theta_\gamma)]$. The shear breaks the azimuthal symmetry of the host lens, which is necessary for it to fit the observed lens position. No attempt is made to incorporate the possible dwarf companion of the lens galaxy that appears as a very faint smudge in the *HST* image. We do not expect that this object is large enough to significantly change the surface potential except in its near vicinity, and the images are well separated from it. In addition, the quality of the fit discussed in § 3.2.1 gives us confidence that the model accurately reproduces the local magnification matrix at the positions of the images, which is the only thing needed here. With the reported redshifts the critical density for this lens is $\Sigma_c = 2.65 \times 10^9\, h_{65}\, M_\odot\,\mathrm{kpc}^{-2}$.

3.2.1. *No Substructure*

A smooth model is fitted to the positions of the lens galaxy, the radio cores of the images, and the center of the jet images. A model is found that fits all the positions to better than 0.1 mas. In addition, the magnification ratio of the radio core agrees with the observed one to better than 10% despite this not being used as a constraint on the model. This signifies that the local magnification matrix $\tilde{\mathbf{A}}$ is being accurately reproduced by the model. The velocity dispersion of the lens is $\sigma_{\mathrm{host}} = 247\ \mathrm{km\ s^{-1}}$, and the background shear is $\gamma = 0.102$. This velocity dispersion is not unusual for a lens galaxy. The estimated circular velocity is $V_{\mathrm{circ}} = \sqrt{2}\sigma_{\mathrm{host}}$. The magnifications at the positions of the radio cores are $\mu_A = 3.8$ and $\mu_B = -1.5$—a negative magnification indicates a one-dimensional parity flip in the image. This model gives a curvature magnification factor of $C = 4.9$ at the center of the jet with image B being the more curved of the two images as observed. If the jet in image A has a curvature of $1/C$ times the curvature in image B and it is in the right direction, then the observations can be explained without substructure. Figure 2 shows some attempts to model the jet in this way. From visual inspection it appears that the jet in image A is not bent enough to explain the bend in image B. The curve should follow the crest of the jet's surface brightness, but a jet that is bent enough requires the end of the jet to be shifted by ~3–4 mas from the crest of the straight jet. The positional uncertainty is dominated by beam smearing, so it is $\sim\sigma_{\mathrm{beam}}/(4\mathrm{SNR})^{1/2}$, where SNR is the signal-to-noise ratio, making the uncertainty in the position of the crest of the jet in the vertical direction (declination) ~0.5 mas. Such a big bend would be easily detected.

Another way of evaluating this is to realize that

$$C \simeq \left(\frac{\theta^A_{\mathrm{jet}}}{\theta^B_{\mathrm{jet}}}\right)^2 \frac{\delta^B}{\delta^A}\ , \tag{15}$$

where θ_{jet} is the length of the jet image and δ is the maximum deviation of the crest from a straight line. Judging from Rusin et al. (2002), $\theta^B_{\mathrm{jet}} \simeq 10$ mas, $\theta^A_{\mathrm{jet}} \simeq 22.0$ mas, and $\delta^B \simeq 2$ mas, giving $\delta^A \simeq 2$ mas with the derived curvature magnification factor. This is around 4 times the positional uncertainty, as estimated above, along the full length of the jet. A more conclusive determination will probably require improved observations.

3.2.2. *Substructure*

The substructure is modeled by adding either SIS or point masses to the smooth model described above. Several different methods for fitting the jet shape were tried. An essential difficulty is that besides the core there are no clear localized features along the jet that can be identified in both images. The positions of these features along with the tangent and curvature at such points could have been used as constraints were they present. Another difficulty arises from the large number of local minima in any χ^2 function that was tried—there are different ways of bending a straight image by either "pushing" or "pulling" at different points.

It was found that the best and most unambiguous results were obtained by first fixing the smooth, or host, lens model to the one discussed in § 3.2.1. A straight line representing the jet in image A is then mapped to image B using the model. The substructures are added near image B by trial and error assisted by minimizing a χ^2 based on the positions of the core and jet center until a curve in image B is obtained that best reproduces the qualitative features of the VLBI map. This method does not use the observed magnification ratio of the cores as a constraint so any possible contamination from microlensing by stars is entirely avoided. Figure 3 shows the results of this fitting. The resulting lens model is not unique in any quantitative sense, but there are clear

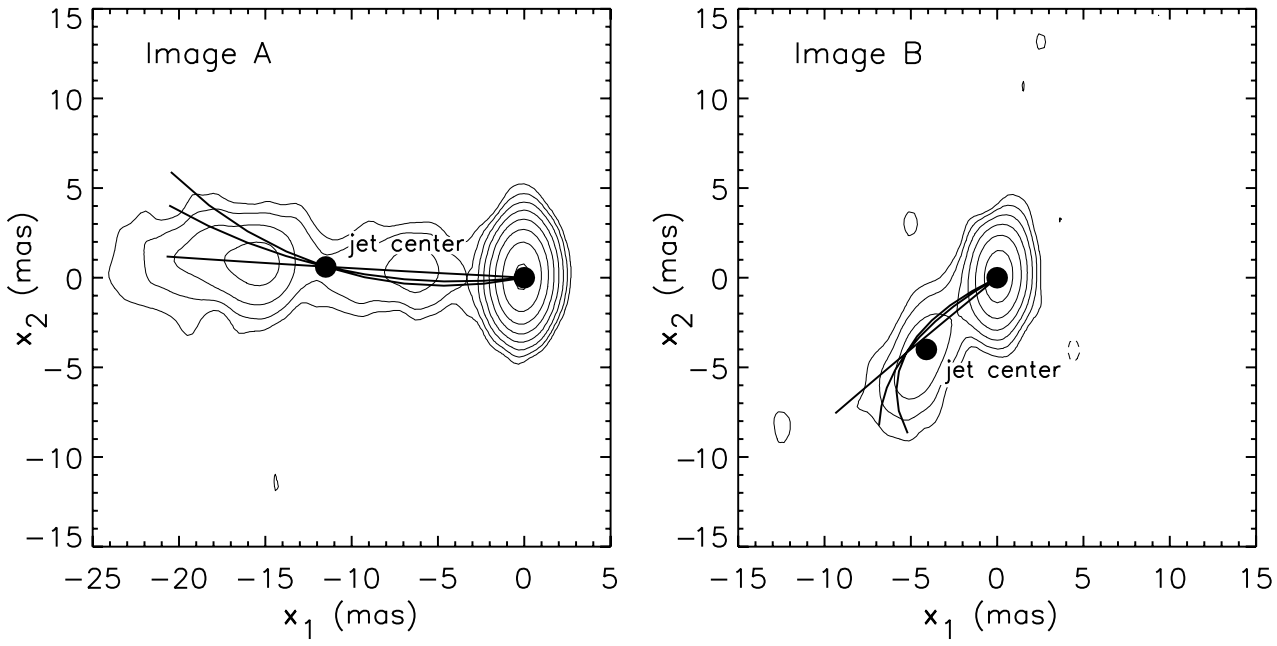

FIG. 2.—Models for the jet shape with no substructure. Using the best-fit smooth model, the arc in image A is mapped onto the B image. The radio core is at the origin in both cases, and the jet center is marked. The three arcs have curvatures of $|\boldsymbol{n}_A| = 0$, 0.029, and 0.043 mas^{-1} in image A and are designed to pass through both the core and the jet center. The model curves are overlaid on the Rusin et al. (2002) VLBI map. The lowest contour is 3 times the rms noise, and each contour is increased by a factor of 2. The beam is 3.6×1.9 with the larger axes being in the vertical x_2 direction.

things that can be learned from this fitting process about the kind of substructure that is capable of producing the bend.

When a point mass is used as a substructure the shape of image B is comparatively easy to reproduce. A point mass can be considered an approximation to any substructure that is very compact relative to its own Einstein radius such as a tidally truncated dark matter halo. Such a substructure can cause a strong deflection near its center while having a limited range of influence. This enables the point mass substructure in Figure 3 to displace the lower end of the jet while leaving the position of the core end of the jet relatively unchanged. Note that the substructure has the effect of

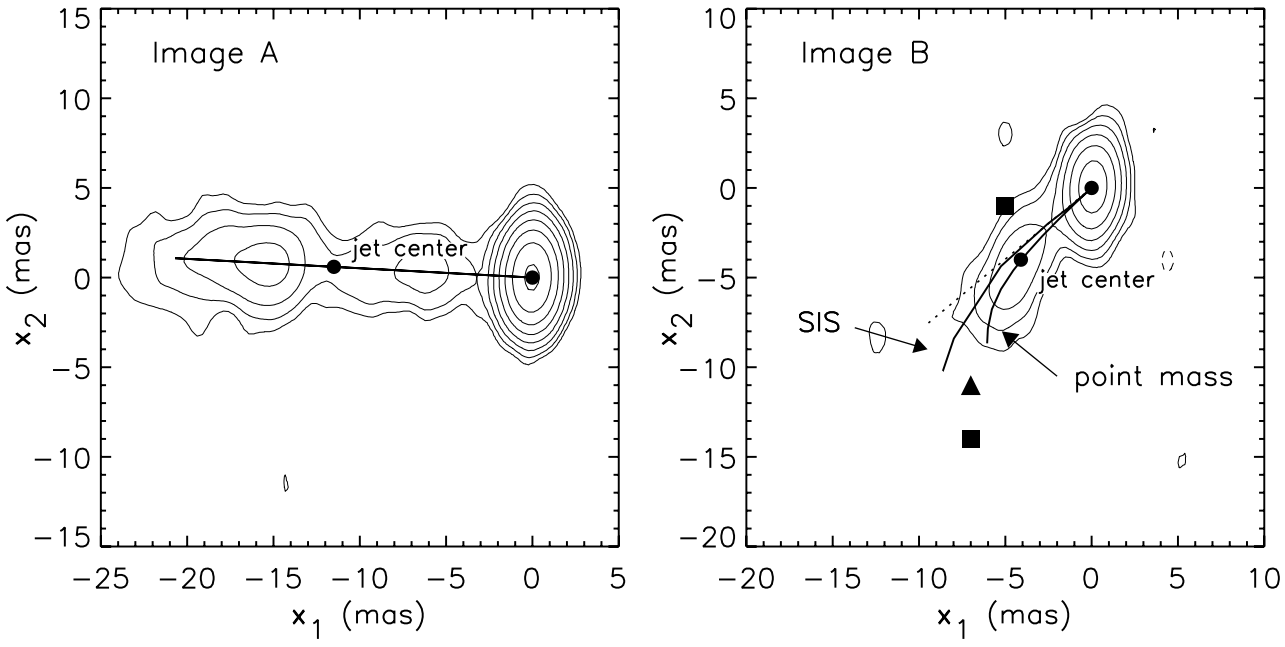

FIG. 3.—Diagrams showing the reconstruction of image B from a line segment representing image A using the two lens models discussed in the text. The position of the point mass substructure is marked by the triangle, and the positions of the SIS substructures are marked by squares. The jets corresponding to each substructure model are marked with arrows. The dotted curve in the right-hand panel is the image without any substructure. In the background are the Rusin et al. (2002) VLBI maps.

attracting the image rather than repelling it, as would normally be the case. This attraction happens in only one dimension and is a result of one of the eigenvalues of the magnification matrix derived from the host lens being negative (image B is reflected in one dimension with respect to image A). The mass is most naturally calculated in units of the mass of the host lens within its Einstein radius, which in this case is $M_{\rm E} = (\sigma/c)^4 G^{-1} \Sigma_c(z_s, z_l)^{-1} = 1.6 \times 10^{11} h_{65}^{-1} (\sigma/247 \text{ km s}^{-1})^4 M_\odot$. The favored model has a substructure mass of $m = 2.5 \times 10^{-5} M_{\rm E}$. Other model parameters are summarized in Table 1. A point mass with mass much more than $10^{-4} M_{\rm E}$ tends to displace the lens without creating a bend, and a mass of $\lesssim 10^{-6} M_{\rm E}$ cannot produce a bend on a large enough angular scale.

When an SIS model is used for the substructure it is difficult to reproduce the jet shape. The tendency is that when the SIS is massive enough to displace the lower end of the jet sufficiently it also displaces the core end of the jet so that a significant bend is not created—i.e., the SIS model is not compact enough. We partially get around this problem by using two SIS substructures in Figure 3 and Table 1, but even this does not produce very satisfactory results, and considering the discussions in § 4, this seems an improbable explanation. It is possible that if the host lens model were allowed to vary along with the sublens model, an explanation could be found that requires only one SIS substructure. However, including the host lens in the fitting process greatly increases the number of local minima in χ^2, and after significant experimentation we have been unable to find a model that is a qualitative improvement on the one in Figure 3 using a single SIS substructure. The two-SIS model requires a precarious balance between the effects of two relatively massive substructures. A small change in the positions or masses causes the jet to be rather drastically distorted. We conclude that substructures as diffuse as SISs are an unlikely explanation for the observations.

By modeling the lens, general conclusions can be made, but the specific form of the substructure is not tightly constrained. This modeling demonstrates that the bend in Q0957+561 can be reproduced by a sufficiently compact substructure. If the host lens model were changed to something other than an SIS+shear model, substructure would still be needed if the jet is truly straight in image A and curved in image B. The new model would also need to reproduce the positions of the center of the jet relative to the core and the magnification ratio of the cores. Because of this the magnification, matrix $\tilde{\mathbf{A}}$ could not be drastically different. The size, position, and structure of the subclumps needed may change somewhat with the host model, but the general conclusions would still be the same.

4. IMPLICATIONS FOR DARK MATTER AND COSMOLOGY

The structures responsible for the bend in image B of B1152+199 and the possible kink in image A of Q0957+561 are not terribly unusual in their mass or size. There are dwarf galaxies and globular clusters orbiting our galaxy that would fit the description. The importance lies in the likelihood of such a structure being close enough to the image to cause observable bending.

4.1. *Estimated Substructure Densities*

To estimate the probability of a jet like the one in B1152+199 having an observable bend, we will consider the bending effect of a single clump acting by itself. The host lens probably enhances the effect of the clump to a small degree. This will not change the results of this section by a large amount and so this extra complication will be neglected.

If we consider a straight line in the source plane that passes by a spherically symmetric lens centered at $\boldsymbol{x}_0$ with an impact parameter of b, the lensing equation (1) can be reduced to

$$b = [r \pm \alpha_r(r)] \cos\theta, \quad r > 0 \,, \tag{16}$$

where $r \equiv |\boldsymbol{x} - \boldsymbol{x}_0|$, θ is the corresponding axial coordinate, and $\alpha_r(r)$ is the radial deflection, which is less than 0. The positive sign is used for $-\pi/2 < \theta < \pi/2$—the primary image—and the negative sign otherwise—the secondary image. We are concerned here only with the primary image; secondary images appear to form rarely in compound lensing with the mass scales considered here (Metcalf & Madau 2001), and they will generally be demagnified.

The curvature of the image can be calculated by taking derivatives of the curve (eq. [16]). At the point $\theta = 0$ the curvature is $\boldsymbol{n}(\theta = 0) = (1/r^2)[(d^2 r/d\theta^2) - r]\hat{\boldsymbol{x}}$. For our two models for the subclump, this is

$$\boldsymbol{n}(\theta = 0) = \frac{-1}{\theta_{\rm E}} \begin{cases} \dfrac{1}{\left(x_b + \sqrt{x_b^2 + 4}\right)^2} \left(\dfrac{3x_b^2 + 8}{\sqrt{x_b^2 + 4}} \right) \hat{\boldsymbol{x}} & \text{(point mass)} \,, \\ \dfrac{1}{(x_b + 1)^2} \hat{\boldsymbol{x}} & \text{(SIS)} \,, \end{cases} \tag{17}$$

where $x_b \equiv b/\theta_{\rm E}$. For the point mass, $\theta_{\rm E} = \left[m/(\pi D_l^2 \Sigma_c)\right]^{1/2}$, and for the SIS, $\theta_{\rm E} = \lambda_{\rm E}(\sigma)/D_l$.

TABLE 1

SUBSTRUCTURE MODEL PARAMETERS

Model	$m/M_{\rm E}$	σ (km s^{-1})	x^1 (mas)	x^2 (mas)	κ	$\mu_{\rm core}$
Point mass	2.5×10^{-5}	...	−7.0	−11.0	0.86	−1.19
SIS	...	9.6	−5.0	−1.0	1.05	−1.07
	...	21.0	−7.0	−14.0	1.05	−1.07

NOTE.—The positions x^1 and x^2 are the center of the substructure with respect to the core in image B. The surface density κ and the magnification $\mu_{\rm core}$ are evaluated at the core in image B.

A clump will not make an observable bend in a jet of length $\theta_{\rm jet}$ if the Einstein ring radius is either too big or too small. From equation (17) we see that the maximum curvature a clump can produce is $\theta_{\rm E}(z)^{-1}$. When $\theta_{\rm E}(z)$ is larger than the length of the jet the deviation from a straight line is at most $\sim\theta_{\rm jet}^2/8\theta_{\rm E}$. This must be larger than the smallest measurable scale, $\theta_{\rm res}$, which is set by either the resolution of the observations or the width of the jet. Applying this criterion to the curvature as a function of b, equation (17) gives an upper limit on the impact parameter. A small clump will influence a region of the jet of size $\sim\theta_{\rm E}$. If the smallest scale $\theta_{\rm res}$ is of order the circumference of the Einstein ring, then its bending effects will be on too small a scale to be observed. These constraints are summarized as

$$\frac{\theta_{\rm res}}{2\pi} \lesssim \theta_{\rm E} \lesssim \frac{\theta_{\rm jet}^2}{8\theta_{\rm res}}, \quad |\boldsymbol{n}(x_b)| \gtrsim \frac{8\theta_{\rm res}}{\theta_{\rm jet}^2} \ . \tag{18}$$

The first of these inequalities can be used to find the range of velocity dispersions or masses that could be responsible an observable bending of the jet in B1152+199:

$$6 \text{ km s}^{-1} \lesssim \sigma \lesssim 13 \text{ km s}^{-1} \ , \tag{19}$$

$$7.1 \times 10^4 \ h_{65}^{-1} \ M_\odot \lesssim m \lesssim 2.7 \times 10^7 \ h_{65}^{-1} \ M_\odot \ , \tag{20}$$

where the values $\theta_{\rm jet} = 15$ mas and $\theta_{\rm res} = 3$ mas have been used. This range is consistent with the σ derived in § 3.2. The true ranges are probably a bit larger because of the influence of the host lens, which will increase the sensitivity to smaller mass objects. The second of the inequalities (eq. [18]) puts an upper limit on the impact parameter b as a function of σ or m through equation (17). By plugging in the smallest allowed clump we can find the largest possible impact parameter—$b \lesssim 1.6$ mas $= 10 \ h_{65}^{-1}$ pc for the SIS and 6.9 mas $= 28 \ h_{65}^{-1}$ pc for the point mass. The clump needs to be quite well aligned with the image.

The probability of a subclump bending the jet will be taken to be $p \propto \theta_{\rm jet} db$ within the allowed range of b. The probability or expected number of important clumps per jet is

$$p \simeq 2\theta_{\rm jet} \frac{c}{H_0} \int_0^{z_s} \frac{dz}{(1+z)} \frac{D(z)^2}{E(z)} \int_{m_{\rm min}(z)}^{m_{\rm max}(z)} \times dm \ b_{\rm max}(m, z) \frac{d\mathcal{N}}{dm}(m, z) \ , \tag{21}$$

where $\mathcal{N}$ is the three-dimensional number density of clumps and $E(z) = [\Omega_m(1+z)^3 + \Omega_R(1+z)^2 + \Omega_\Lambda]^{1/2}$, $\Omega_R = 1 - \Omega_m - \Omega_\Lambda$. In the case of SIS lenses m can be replaced with σ and $b_{\rm max}(\sigma, z)$ can be found explicitly. For the point mass case, $b_{\rm max}(m)$ must be found numerically.

To get a simple estimate of the number density of clumps required, we can take them to all lie within the host lens and give them all the same velocity dispersion. In this case equation (21) reduces to

$$p \simeq 2\theta_{\rm jet}^2 D_l^2 \eta(\sigma) \left[\sqrt{\frac{2\theta_{\rm E}(\sigma)}{\theta_{\rm res}}} - \frac{\theta_{\rm E}(\sigma)}{\theta_{\rm jet}} \right] \ (\text{SIS}) \ , \tag{22}$$

where $\eta(\sigma)$ is the two-dimensional number density of clumps. The range of allowed σ given in equation (19) gives a range $\eta(\sigma)/p \simeq 32$–$111 \ h_{65}^2$ kpc^{-2}. This is the number density of substructures required to make the bending commonplace. The same exercise with point masses in the range $m = 10^5$–$10^7 \ M_\odot$ gives a range of $\eta(\sigma)/p \simeq 130$–$260 \ h_{65}^2$ kpc^{-2} or $\Sigma = 1.3 \times 10^7$–$2.6 \times 10^9 \ M_\odot$ kpc^{-2}, where the higher mass density is for larger mass clumps. In units of the critical density this is $\kappa = 0.005$–0.99. This value is anywhere from a few percent to more than all of the surface density of the host lens. The lensing effect of the host lens may reduce these estimates by a factor of roughly $|\mu|^{-1/2}$—an estimate of the eigenvalues of the magnification matrix—which is 0.3–0.9 for the model found in § 3.2.

Instead of fixing the mass of the substructure, we can guess at a realistic mass function. One expects that the number density of small mass clumps will be proportional to the density of all matter ρ averaged over a larger scale than the clumps being considered—constant Lagrangian number density. CDM simulations and analytic estimates predict a power-law mass function for the low-mass range important here,

$$\frac{1}{\rho}\frac{d\mathcal{N}}{dm} = \frac{1}{M_0 m_0}\left(\frac{m}{m_0}\right)^\alpha \ , \tag{23}$$

where m_0 and M_0 are normalization constants. Fitting the mass function from ΛCDM N-body simulations to the observed velocity distribution in the range $V_{\rm circ} = 20$–400 km s^{-1} gives the relation $\sigma \simeq 100$ km s^{-1} $(m/3.0 \times 10^{11} \ M_\odot)^{1/3}$. For SIS substructures, this relation is used to convert equation (23) into a distribution of velocity dispersions where it is extrapolated below $V_{\rm circ} = 20$ km s^{-1}. In ΛCDM simulations the dark matter clumps have $\alpha \simeq -1.91$ and $M_0 = 4.8 \times 10^{12} \ h^{-1} \ M_\odot$ for $m_0 = 3.0 \times 10^{11} \ M_\odot$ (Klypin et al. 1999). The exponent for the σ distribution is $\alpha_\sigma = -3.73$ in this case. This distribution fits the observed distribution of dwarf galaxies near $\sigma = 50$–100 km s^{-1} above which the contribution to equation (21) is small.

Using the full range of masses in equation (19) and keeping all the subclumps at the redshift of the host lens results in a probability of $p \simeq 3.2\kappa$, where κ is the surface density of the host lens, $\kappa = 0.35$ and 0.85 for the model in § 3.2. Figure 4 shows p and the fraction of the halo mass density contained in substructure as a function of a lower mass cutoff in the mass function. The smaller mass clumps contribute most of the probability but little of the mass density. This mass fraction is a lower limit in that if the internal structure of the subclumps is less centrally concentrated, it will require more mass to reach the same probability. For SIS substructures that are not tidally truncated, $p = 1.9 \times 10^{-3}\kappa$. To increase this probability by a factor of 10 would require the entire mass density of the host lens to be composed of SISs in the range of equation (19). Any tidal truncation will reduce SIS substructures' lensing effect.

Objects that are not in the host galaxy but happen to lie near the line of sight could also cause bending of the jet. To estimate this contribution, we integrate equation (21) with the mass function equation (23) assuming that ρ along the line of sight is given by the average density of the universe. For SIS structure, $p = 1.3 \times 10^{-4}$, and for point masses with the same mass function, $p = 0.65$. This extragalactic population is only an important contribution to the probability if the clumps are very compact, in which case it is comparable to the contribution from substructures inside the lens.

The CDM model does seem capable of accounting for the bent jets, provided that DM halos are relatively compact. If the radius is small compared to the Einstein radius of a

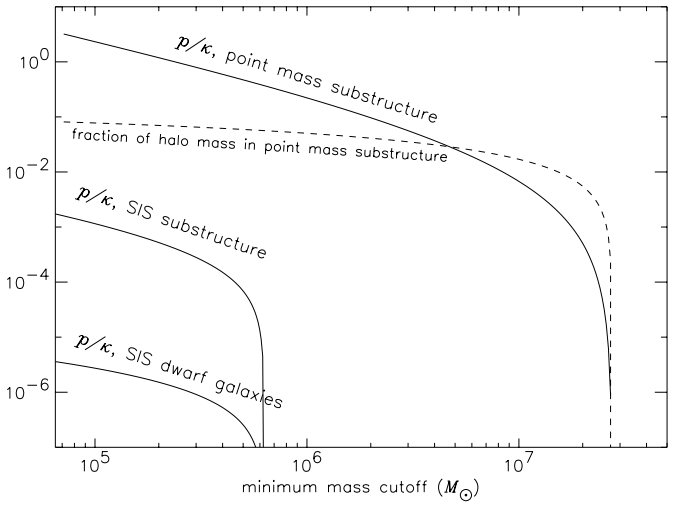

FIG. 4.—Probability of substructures causing an observable bend in a radio jet like the one in B1152+199 assuming the distribution of substructures described in the text. For the SIS substructures, the velocity dispersion is converted to mass by $m = 3.0 \times 10^{11}\ M_\odot(\sigma/100\ \mathrm{km\ s^{-1}})^3$. The fraction of the host halo surface density contained in point mass substructure is also plotted. The host lens surface density is $\kappa = 0.6$–1.4 for the model of B1152+199 discussed in § 3.2.

point mass of the same mass [$r \lesssim \theta_E = 11(m/10^6\ M_\odot)^{1/2}\ h_{65}^{1/2}$ pc], less than ~10% of the mass need be in substructure. However, any less concentrated clumps will require more total mass. The SISs require much more mass. The Navarro, Frenk, & White (NFW) profile (Navarro, Frenk, & White 1997), $\rho(r) = \rho_c r_s^3 r^{-1}(r_s + r)^{-2}$, is believed to be more realistic for pure dark matter halos. If r_s is small compared to the above limit and a large fraction of the mass is within this radius, then the mass fraction might get down to the levels shown in Figure 4. The scale length according to the standard structure formation scenario is $r_s = 2.17 \times 10^3 c^{-1}\ h_{65}^{-2/3}(m_{200}/10^6\ M_\odot)^{1/3}$ pc, where c is the concentration and m_{200} is the virial mass. If the concentration is 100 or larger, then the core is compact enough, but in this case the mass within r_s is less than 10% of m_{200}. In addition, $c \simeq 100$ is a bit high for a straightforward extrapolation of the simulations (Bullock et al. 2001)—no simulation has been done with a resolution high enough to resolve these mass scales. To achieve the same probability for bending the jet, it seems that any realistic CDM model will require significantly more mass—at least before tidal stripping occurs—to be in small-scale structure than is required in the point mass model used here.

Also, the survival of substructure in the host lens is a complicated issue. Clumps with $m \gtrsim 10^7\ M_\odot$ are not likely to survive within the inner few kiloparsecs because they lose orbital energy to dynamical friction and fall into the center of the galaxy where they are destroyed by tides. This upper mass cutoff can significantly change the local fraction of mass in substructures while not affecting the lensing probability greatly.

4.2. *Contribution from Known Structures*

There are about 40 known dwarf galaxies in the Local Group (Mateo 1998; Klypin et al. 1999). Most of these are within ~300 kpc of either the MW or M31. About 28 of these have circular velocities above 10 km s^{-1}. This gives an estimated surface number density of $\sim 3.5 \times 10^{-5}$ kpc^{-2} if they were uniformly distributed in this volume. There are about 200 globular clusters in the MW with masses of 10^4–$10^6\ M_\odot$, making their number density an order of magnitude larger. The concentration of dwarfs and globular clusters toward the center of the galaxy and observational incompleteness might increase this estimate by a factor of several, but nowhere near enough to reach the required number densities derived in the previous section.

Another way of estimating the contribution from dwarf galaxies is to use the mass function (eq. [23]) converted to velocity dispersion. For the observed galaxies within 200 h^{-1} kpc of the MW and M31, $\alpha_\sigma = -2.35 \pm 0.4$ and $m_0 \simeq M(<200)/6.32$ for $\sigma_0 = 10$ km s^{-1}, where $M(<200)$ is the total mass within 200 h^{-1} kpc (Klypin et al. 1999). We will use $M(<200) = 10^{12}\ M_\odot$. With SIS dwarf galaxies this velocity distribution gives a probability for bending the jet of $p = 3.9 \times 10^{-6}\kappa$ if the dwarfs are in the host lens. Figure 4 shows p as a function of a lower σ cutoff, which is converted into mass by $\sigma = 100\ \mathrm{km\ s^{-1}}(m/3.0 \times 10^{11}\ M_\odot)^{1/3}$. If the same velocity distribution is used for the entire line of sight at the average mass density, $p = 2.7 \times 10^{-7}$. Dwarf galaxies are not compact enough to be considered point mass lenses, but by treating them as point masses we can get an (probably greatly inflated) upper limit on the probability. In this case $p = 8.9 \times 10^{-5}\kappa$.

Known types of substructure within the host lens are inadequate to explain B1152+199. If the structures in the lens and in intergalactic space are similar in number and central density to those observed in the Local Group of galaxies, they fall short of the estimates derived in § 4.1 by at least a factor of 10^5.

5. DISCUSSION

These observations have important consequences for the WDM model. The standard WDM model is engineered to reproduce the dwarf galaxy distribution under the assumption that a galaxy forms in every small halo. It was shown in § 4.2 that the number density of dwarf galaxies is extremely unlikely to have produced the observed bent radio jets. The standard WDM model is thus ruled out if the bend in B1152+199 is real. A more accurate lower limit on the DM particle mass will require more observations and more simulations of small-scale structure formation in these models.

Higher resolution observations of B1152+199 are possible. These would make certain that the jet in image B is indeed bent and improve the constraints on the substructure mass. Also interesting would be high-resolution images of other multiply imaged jets. In the present sample of three all appear to show some evidence of bending. A moderately larger sample would greatly increase the power of this method to probe structure on small scales. It is possible that scattering by compact ionized regions in the lens galaxy could affect the jet morphologies. There is no evidence for this in B1152+199, but in general this effect would be wavelength dependent so observations at multiple frequencies would very useful.

It has been found here that a significantly larger number of small-scale objects are needed if the observations of B1152+199 are to be simply interpreted. Structures as diffuse as SIS are disfavored both by direct modeling of B1152+199 and on statistical grounds. If the structures are compact (on the scale of their own Einstein radius) and small in mass ($\lesssim 10^7\ M_\odot$), they need not contain a large frac-

tion of the mass in the universe. However, such concentrated halos come about in the CDM model only through the tidal stripping of halos that originally contained $\sim$10 times more mass. This means that in intergalactic space these clumps would contain a large fraction of the mass, perhaps most of it.

I would like to thank P. Madau, M. Magliocchetti, H. Zhao, and the anonymous referee for useful discussions and comments. Special thanks to D. Rusin for bringing the case of B1152+199 to my attention and providing the VLBI maps.

REFERENCES

Barkana, R., Lehár, J., Falco, E. E., Grogin, N. A., Keeton, C. R., & Shapiro, I. I. 1999, ApJ, 520, 479
Blandford, R. D., & Jaroszynski, M. 1981, ApJ, 246, 1
Bode, P., Ostriker, J. P., & Turok, N. 2001, ApJ, 556, 93
Bradač, M., Schneider, P., Steinmetz, M., Lombardi, M., King, L. J., & Porcas, R. 2002, A&A, 388, 373
Bullock, J. S., Kolatt, T. S., Sigad, Y., Somerville, R. S., Kravtsov, A. V., Klypin, A. A., Primack, J. R., & Dekel, A. 2001, MNRAS, 321, 559
Bullock, J. S., Kravtsov, A. V., & Weinberg, D. H. 2000, ApJ, 539, 517
Chiba, M. 2002, ApJ, 565, 17
Dalal, N., & Kochanek, C. S. 2002, ApJ, 572, 25
Garrett, M. A., Calder, R. J., Porcas, R. W., King, L. J., Walsh, D., & Wilkinson, P. N. 1994, MNRAS, 270, 457
Irwin, M. J., Webster, R. L., Hewett, P. C., Corrigan, R. T., & Jedrzejewski, R. I. 1989, AJ, 98, 1989
Kamionkowski, M., & Liddle, A. 2000, Phys. Rev. Lett., 84, 4525
Keeton, C. 2002, in The Mass of Galaxies at Low Redshift, ed. R. Bender & A. Renzini, press
Kemball, A. J., Patnaik, A. R., & Porcas, R. W. 2001, ApJ, 562, 649
King, L. J., Browne, I. W. A., Muxlow, T. W. B., Narasimha, D., Patnaik, A. R., Porcas, R. W., & Wilkinson, P. N. 1997, MNRAS, 289, 450
Klypin, A., Kravtsov, A. V., Valenzuela, O., & Prada, F. 1999, ApJ, 522, 82
Koopmans, et al. 1999, MNRAS, 303, 727
Mao, S., & Schneider, P. 1998, MNRAS, 295, 587
Marlow, et al. 2001, AJ, 121, 619
Mateo, M. L. 1998, ARA&A, 36, 435
Metcalf, R. 2002, in Where's the Matter?, ed. L. Tresse & M. Treyer, in press
Metcalf, R. B., & Madau, P. 2001, ApJ, 563, 9
Metcalf, R. B., & Zhao, H. 2002, ApJ, 567, L5
Moore, B., Ghigna, S., Governato, F., Lake, G., Quinn, T., Stadel, J., & Tozzi, P. 1999, ApJ, 524, L19
Myers, S. T., et al. 1999, AJ, 117, 2565
Navarro, J. F., Frenk, C. S., & White, S. D. M. 1997, ApJ, 490, 493
Ros, E., Guirado, J. C., Marcaide, J. M., Pérez-Torres, M. A., Falco, E. E., Muñoz, J. A., Alberdi, A., & Lara, L. 2000, A&A, 362, 845
Rusin, D., Norbury, M., Biggs, A. D., Marlow, D. R., Jackson, N. J., Browne, I. W. A., Wilkinson, P. N., & Myers, S. T. 2002, MNRAS, 330, 205
Rusin, D., et al. 2001, AJ, 122, 591
Somerville, R. S. 2002, ApJ, 572, L23
Spergel, D. N., & Steinhardt, P. J. 2000, Phys. Rev. Lett., 84, 3760
van den Bosch, F. C., Robertson, B. E., Dalcanton, J. J., & de Blok, W. J. G. 2000, AJ, 119, 1579
Walsh, D., Carswell, R. F., & Weymann, R. J. 1979, Nature, 279, 381
Wambsganss, J., & Paczynski, B. 1992, ApJ, 397, L1
Witt, H. J., Mao, S., & Schechter, P. L. 1995, ApJ, 443, 18
Woźniak, P. R., Alard, C., Udalski, A., Szymański, M., Kubiak, M., Pietrzyński, G., & Zebruń, K. 2000, ApJ, 529, 88
Xanthopoulos, E., et al. 2000, in Proc. 5th European VLBI Network Symposium, ed. J. E. Conway, A. G. Polatidis, R. S. Booth, & Y. M. Pihlström (Göteborg: Onsala Space Observatory), 49